Journal of Materials Chemistry A

ROYAL SOCIETY OF CHEMISTRY

PAPER

View Article Online
View Journal | View Issue

Cite this: J. Mater. Chem. A, 2026, 14, 9619

Mechanistic insights into CO_2 capture and electrochemical conversion in nonaqueous Na–CO_2 batteries

Rahul Jayan, †[b] Satheesh Mani †[a] and Md Mahbubul Islam *[a]

Received 26th November 2025
Accepted 12th January 2026

DOI: 10.1039/d5ta09674j

rsc.li/materials-a

Developing efficient energy storage systems that capture and convert CO_2 is critical for mitigating carbon emissions. Here, we report a Na–CO_2 battery with ruthenium dioxide (RuO_2) cathode catalysts and propane-1,3-diamine (PDA) as an electrolyte additive to enhance CO_2 capture and conversion efficiency. The integration of CO_2 adsorption and electrochemical reduction facilitates activation of the inert CO_2 molecule and circumvents gas–solid–liquid ternary-phase reactions at the interface. We employed density functional theory (DFT) calculations to systematically unravel the reaction mechanisms and energetics governing CO_2 reduction, both with and without PDA. Our results reveal an energetically favorable pathway toward the formation of Na_2CO_3 and C as final discharge products, rather than sodium oxalate ($Na_2C_2O_4$). The CO_2–amine adduct facilitates charge transfer from PDA to CO_2, which results in activation of CO_2. The kinetics of CO_2 conversion and regeneration of PDA were found to be significantly enhanced on the RuO_2 surface compared to the bulk electrolyte. More importantly, pre-activation of CO_2 *via* the amine–CO_2 adduct lowers the total overpotential to 2.44 V, compared to 3.13 V without PDA. This study provides fundamental insights into CO_2 electroreduction in Na–CO_2 batteries and underscores the promise of electrolyte engineering for sustainable CO_2 utilization and high-performance energy storage.

1. Introduction

The industrial revolution and globalization have resulted in massive emissions of CO_2 gas due to the extensive consumption of fossil fuels.[1] One approach focuses on minimizing fossil fuel dependence by improving energy efficiency and transitioning to renewable energy sources, such as wind, solar, hydropower, and biomass, alongside the use of green hydrogen generated from renewable electricity. Additionally, capturing and storing CO_2 emissions from industrial processes and power generation through methods such as geological storage in depleted oil and gas fields or beneath the ocean floor presents a possible solution. However, the complete mitigation of CO_2 emissions remains an elusive goal because of the ongoing reliance on fossil fuels and the associated technological and economic barriers. As such, carbon capture and storage technologies have emerged as essential tools for mitigating CO_2 emissions through the capture and sequestration of carbon from industrial sources, thus preventing its release into the atmosphere.

Extensive efforts have been dedicated to advancing post-combustion carbon capture technologies, with aqueous amine solutions such as monoethanolamine (MEA) representing the most industrially developed systems.[2,3] The main challenge limiting carbon capture technologies is the high energy needed for CO_2 regeneration, where heat is used to release CO_2 from the capture medium. This process can consume up to 30% of a power plant's energy output, which significantly reduces the efficiency and makes large-scale adoption less practical.[4,5] Despite the advantages of amine-based CO_2 capture, such as industrial maturity and adaptability, the challenges associated with geological storage and its low efficiency necessitate alternative approaches. In this context, electrochemical CO_2 reduction has emerged as the most promising approach due to its energy efficiency, scalability, and direct integration with renewable energy sources. Additionally, electrochemical conversion processes operate under mild conditions and offer an attractive solution for mitigating carbon emissions in a sustainable and practical manner.[6–8] This approach efficiently transmutes sequestered CO_2 into valuable products such as fuels (*e.g.*, methane) and chemicals (*e.g.*, formic acid),[9] thereby eliminating the need for prolonged CO_2 storage by converting captured CO_2 into usable materials. Overall, electrochemical CO_2 reduction offers a sustainable, energy-efficient, and scalable alternative for addressing CO_2 emissions.[5,9]

Within the realm of electrochemical CO_2 reduction, metal–CO_2 batteries such as Li-, Na-, Zn-, and K–CO_2 systems offer high energy density and the dual benefit of energy storage and

[a]Department of Mechanical Engineering, Wayne State University, Detroit, Michigan 48202, USA. E-mail: gy5553@wayne.edu
[b]Theoretical Division, Los Alamos National Laboratory, Los Alamos, NM 87544, USA
† These authors contributed equally to this work.

CO_2 fixation and conversion.[10,11] In such systems, CO_2 is electrochemically reduced in a gas cathode coupled with alkali/alkaline metal anodes and organic electrolytes.[5,12] Among these, Na–CO_2 batteries have garnered significant attention due to the abundance, low cost, and lithium-like physicochemical properties of sodium, which make it a sustainable and economically attractive alternative for energy storage.[13–15] These batteries offer superior overall performance, such as a high energy density of 1.13 kWh kg^{-1} and a relatively high operating voltage of 2.35 V.[13,16] Besides, the lower Gibbs free energy ($\Delta G^0 = -905.6$ kJ mol^{-1}) for the reaction between Na and CO_2 results in a reduced charge potential compared to Li ($\Delta G^0 = -1081$ kJ mol^{-1}).[13,17] This lower charge potential minimizes the risk of electrolyte decomposition, thereby enhancing round-trip energy efficiency and extending the operational lifespan of Na–CO_2 batteries. Additionally, Na^+ ions offer distinct benefits over Li^+ ions. Due to their larger ionic radius, Na^+ ions exhibit lower polarization and higher coordination numbers, which facilitate improved charge transport. Furthermore, their reduced solvation energy results in lower charge transfer resistance and accelerated electrode kinetics, positioning Na–CO_2 batteries as a promising alternative for efficient and sustainable energy storage solutions.[17–19]

Recent studies have explored various cathode–electrolyte configurations to improve the electrochemical performance of Na–CO_2 batteries. For example, Na–CO_2 batteries utilizing multi-walled carbon nanotubes with ether-based electrolytes have demonstrated a reversible capacity of 60 000 mAh g^{-1} at 1 A g^{-1} and retained a capacity of 2000 mAh g^{-1} at a charge voltage of <3.7 V for 200 cycles.[17] Thoka *et al.* reported that a Na–CO_2 battery employing a $ZnCo_2O_4$@CNT air cathode with 1 M $NaClO_4$/tetraethylene glycol dimethyl ether (TEGDME) electrolyte showed a charge overpotential of 3.8 V with a limited capacity of 500 mAh g^{-1} at 100 mA g^{-1} over 150 cycles.[20] Despite the use of viable solvents such as dimethyl ether (DME) and dimethyl sulfoxide (DMSO), direct CO_2 reduction faces significant challenges due to its slow kinetics. This process demands the activation of the thermodynamically stable CO_2 molecule to form a highly reactive CO_2^- anion radical intermediate.[21–23] Scientists have been working intensively to find an alternative approach to resolve the CO_2 activation issue. Gallant *et al.* proposed a methodology that integrates electrochemical techniques into carbon capture and storage systems to address the performance and efficiency challenges.[24] It involves introducing CO_2 gas to react with an amine solution, forming an adduct in which the CO_2 molecule bonds with the amine's nitrogen atom. This reaction transforms CO_2 from a stable, linear structure to a reactive, negatively charged bent configuration, primed for further reactions. Gallant *et al.*'s innovative method uses electrochemistry to cleave the CO_2^-amine adduct at the carbon–nitrogen bond. This process results in the amine being regenerated to its original, unreacted state, and ready to capture additional CO_2. Simultaneously, the bent, chemically reactive CO_2 is released near the electrode for electroreduction. During battery discharge, this reactive CO_2 interacts with electrons and lithium cations. This reaction ultimately leads to the formation of lithium carbonate (Li_2CO_3), which then deposits on the carbon electrode.[25]

In this study, we aimed to understand the capture of CO_2 using amines such as propane-1,3-diamine (PDA) and its subsequent reduction on a catalytic cathode. To the best of our knowledge, no detailed computational studies, such as those based on density functional theory (DFT), have been conducted on the use of PDA for CO_2 capture and utilization in Na–CO_2 batteries. The goal of our work is to systematically investigate and compare the kinetics of CO_2 activation with and without using PDA amine on the RuO_2 catalyst, as well as the detailed mechanism of PDA regeneration through post-CO_2 release near the cathode (*i.e.*, RuO_2 catalyst) in the Na–CO_2 system. RuO_2 has demonstrated remarkable catalytic activity in various systems, including Li–CO_2 batteries, the nitrogen reduction reaction (NRR), oxygen evolution/reduction reactions (OER/ORR), CO_2 reduction, and the hydrogen evolution reaction (HER).[26–31] Its high electronic conductivity, significant CO_2 affinity, and catalytic stability for multi-electron reactions make it a suitable cathode catalyst for Na–CO_2 batteries. Building on our previous work on the Mg–CO_2 battery, where RuO_2 served as an efficient cathode catalyst, providing abundant adsorption sites and enhanced accessibility for reaction processes with an observable overpotential of 2.65 V,[32] we were motivated to further investigate its catalytic performance in the Na–CO_2 system. Furthermore, we analyze the Gibbs free energies of various intermediate pathways for $Na_2C_2O_4$ and Na_2CO_3 + CO nucleations to investigate the mechanisms leading to the formation of the final discharge products in Na–CO_2 batteries. Additionally, we elucidate the electrochemical free energies for the most preferred reaction pathway to examine how the RuO_2 catalyst with and without PDA amine contributes to enhancing the electrochemical performance of nonaqueous Na–CO_2 batteries.

2. Computational methodology

The Vienna *Ab initio* Simulation Package (VASP) was used for all first-principles DFT computations.[33] The generalized gradient approximation (GGA) in the form of the Perdew–Burke–Ernzerhof (PBE) functional was employed to describe exchange–correlation effects.[34] The projector augmented wave (PAW) approach was used to treat the interaction between core and valence electrons. The surface model was based on a five-layer slab of RuO_2 (211), constructed using bulk-optimized DFT lattice parameters. The (211) surface of rutile RuO_2 was found to be stable with the lowest surface formation energy, as per previous HRTEM and XRD investigations.[31,35] A 20 Å vacuum layer was included perpendicular to the slab to prevent artificial periodic interactions. To approximate surface atomic dynamics, the top three layers of the slab were fully relaxed during structural optimization, while the bottom two layers were fixed. The plane-wave energy cutoff was set at 500 eV. Brillouin zone sampling was performed using a Monkhorst–Pack *k*-point mesh of $3 \times 3 \times 1$ for surface calculations. Structural optimizations were continued until the residual forces on each atom were less than 0.025 eV $Å^{-1}$, and electronic self-consistency was achieved with an energy convergence criterion of 10^{-5} eV. Bader analysis

was conducted to quantify the amount of charge transfer between the RuO_2 substrate and adsorbed intermediates (Na, CO_2, $Na_2C_2O_4$, and Na_2CO_3 + CO), with the difference in charge density calculated using the specified equation:

$$\rho_b = \rho_{\{\text{adsorbed state}\}} - (\rho_{\{\text{adsorbate}\}} + \rho_{\{\text{AM}\}}) \quad (1)$$

where $\rho_{\text{adsorbed state}}$, $\rho_{\text{absorbate}}$, and ρ_{AM} represent the charge density of the adsorbed intermediates on RuO_2, the isolated intermediates, and the substrate (RuO_2), respectively.

Implicit solvation calculations were performed using the VASPsol[36] module within the framework of DFT, as implemented in the VASP package, to investigate the thermodynamics of amine regeneration *via* N–C bond cleavage in the presence of an organic solvent, di-methoxy ethane (DME). The solvent environment was modeled using a dielectric continuum with a dielectric constant of 7.2,[37] where the solute was treated quantum mechanically and the solvent as a polarizable continuum. Ionic screening effects were excluded, and cavitation energy contributions were neglected. For isolated molecular species, including RNH_2, RNHCOOH, $RNHCOO^-$, RNH_3^+, $NaCO_2$, and RNHCOONa, large simulation cells were employed to avoid interactions between periodic images, and Brillouin zone sampling was restricted to the Γ-point. For electrode–electrolyte interface models involving the RuO_2 substrate, a denser k-point mesh of $5 \times 5 \times 1$ was used to ensure accurate Brillouin zone sampling. We used VASPKIT[38] to calculate the Gibbs free energy (ΔG) for each reaction intermediate step in the Na–CO_2 discharge process, by using the equation $\Delta G = \Delta E + \Delta ZPE - T\Delta S$ at 298.15 K. In this equation, ΔE represents the adsorption energy, and ΔZPE and $T\Delta S$ represent the differences in zero-point energy and entropy between the gas and adsorbed phases. The atomic visualization and charge density differences were carried out with the VESTA code.[39] Besides, geometry optimization was performed for isolated CO_2, PDA, and the CO_2-PDA adduct using Gaussian 16 (G-16) software[40] by employing the B3LYP exchange–correlation functional in combination with the 6-311++G(d,p) basis set. After geometry optimization, the Natural Bonding Orbital (NBO) analysis was carried out to evaluate the electronic interaction between CO_2 and PDA.

3. Results and discussion

3.1. Mechanisms of $Na_2C_2O_4$ and Na_2CO_3 + CO nucleation

The nonaqueous Na–CO_2 battery consists of a sodium metal anode, a separator, organic electrolytes, a porous cathode, and suitable catalysts, such as RuO_2. During discharge, Na undergoes oxidation at the anode, releasing Na^+ ions and electrons. The Na^+ ions then diffuse through the electrolyte to the CO_2 cathode, driven by the potential difference between the electrodes. Concurrently, CO_2 molecules dissolved in the electrolyte adsorb onto the cathode, where they receive electrons from the external circuit and react with Na^+ ions to form solid discharge products, such as Na_2CO_3 + CO or $Na_2C_2O_4$, at the cathode/electrolyte interface. Several experimental studies reported different end discharge products depending upon the choice of cathode catalyst. For instance, X-ray photoelectron spectroscopy (XPS) analysis on a nitrogen-doped nanocarbon (NC900) cathode revealed a CO_3^{2-} signal after discharge, which disappeared upon charging, confirming the reversible formation and decomposition of Na_2CO_3.[41] Furthermore, Xu *et al.*'s work on Co-encapsulated N-doped carbon frameworks (Co-NCFs) demonstrated enhanced formation of highly reversible $Na_2C_2O_4$ as a discharge product.[42] *Ex situ* XPS characterization revealed the emergence of a new peak corresponding to the C–C bond of $C_2O_4^{2-}$ at 893 cm^{-1}, which increased in intensity with extended discharge time, indicating the formation of $Na_2C_2O_4$.[42] This peak disappeared during the subsequent charging cycle, confirming the reversible nature of $Na_2C_2O_4$. Among that, Na_2CO_3 is generally considered to be the thermodynamically stable and final discharge product on the majority of catalytic surfaces in Na–CO_2 batteries.[41] According to earlier experimental research, Na_2CO_3 can be formed directly from CO_2 reduction or indirectly *via* an oxalate-mediated route. In the indirect process, $Na_2C_2O_4$ originates as an intermediate and then breaks down into Na_2CO_3 and CO, while in the direct approach, electrochemical reduction of CO_2 results in the formation of direct Na_2CO_3 together with CO evolution, as shown in the following equations.

(a) Direct pathway

$$2Na\ (s) + 2CO_2\ (g) \rightleftharpoons Na_2CO_3\ (s) + CO\ (g) \quad (2)$$

(b) Indirect pathway *via* oxalate formation

$$2Na\ (s) + 2CO_2\ (g) \rightleftharpoons Na_2C_2O_4\ (s) \rightleftharpoons Na_2CO_3\ (s) + CO\ (g) \quad (3)$$

In this section, the free energy profiles for reaction pathways including direct and indirect Na_2CO_3 formation at open circuit ($U = 0$ V) and equilibrium ($U = U_0$) potentials are explored to determine the most energetically favored pathway resulting in carbonate production. The schematic representations of these pathways are illustrated in Fig. 1. More importantly, the electrochemical discharge stage primarily produces Na_2CO_3 + CO, and the subsequent conversion of CO into elemental carbon is considered as a secondary chemical process that occurs after electrochemical discharge. So, this work majorly focuses on the energetics and surface interactions that drive CO_2 electroreduction leading to the formation of Na_2CO_3 + CO.

Our calculations reveal that both Na and CO_2 spontaneously adsorb onto the RuO_2 substrate, with binding energies of −1.08 eV and −0.23 eV, respectively. Na prefers to adsorb at the hollow site coordinated by Ru and O atoms, while CO_2 predominantly adsorbs on the top of the Ru atom, consistent with previous studies on Mg and CO_2 adsorption on RuO_2.[32] The strong adsorption of both Na and CO_2 is crucial for overcoming the thermodynamic stability of CO_2 and initiating the electrochemical reduction process. Interestingly, our analysis reveals that initial CO_2 adsorption on RuO_2 does not induce its activation. The CO_2 molecule retains its linear structure with minimal changes in bond angle (178.8°), suggesting that direct adsorption alone does not activate CO_2. The first step in the catalytic cycle, therefore, involves Na adsorption, which is

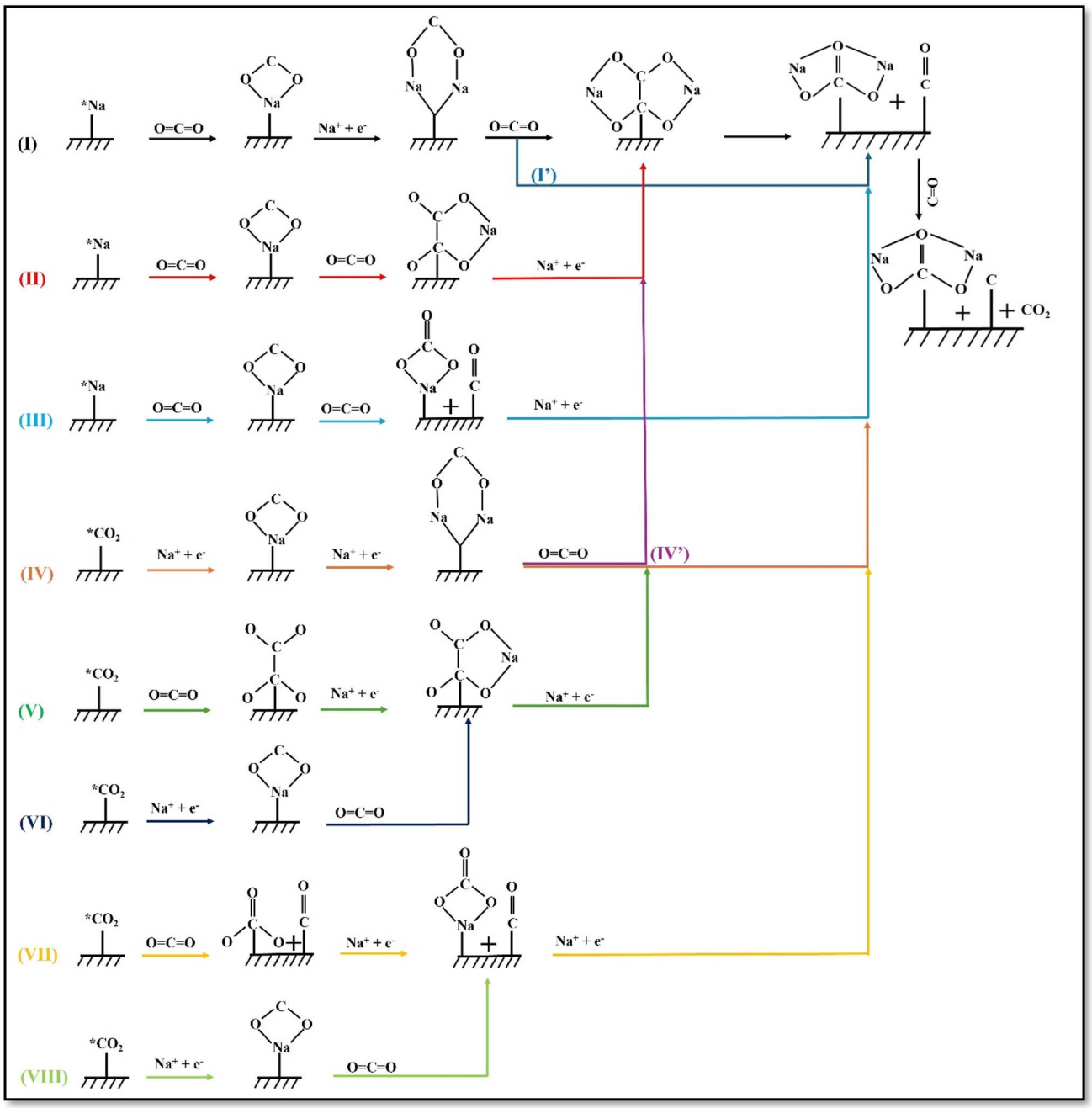

Fig. 1 Schematic illustration of the free energy pathway for CO_2 reduction, leading to the formation of the final discharge product.

pivotal for facilitating CO_2 activation. Upon Na adsorption, the CO_2 molecule undergoes a pronounced structural rearrangement, with the bond angle reduced to 141°, signaling its activation. This activation mechanism, induced by alkali metal adsorption, is consistent with previous observations in Mg–CO_2 systems on RuO_2, which explain the role of Na in promoting CO_2 activation.[32] This step is essential for overcoming the inherent stability of CO_2 and initiating the subsequent reduction steps on RuO_2 catalysts.

The Gibbs free energy profiles presented in Fig. 2(a and b) depict the various reaction pathways leading to the formation of Na_2CO_3 + CO as discharge products on a RuO_2 (211) catalyst at U = 0 V. Notably, in the Gibbs free energy profiles for both the direct Na_2CO_3 + CO pathway (Paths I′, III, IV′, and VIII) and the Na_2CO_3 + CO formation pathway *via* the $Na_2C_2O_4$ intermediate (Paths I, II, IV, and VI), all steps involving Na^+ coupled with electron transfer are downhill on the catalyst surface. Interestingly, both possible sequences such as Na adsorption followed by CO_2 adsorption and CO_2 adsorption followed by Na adsorption exhibit exothermic behavior. The free energy value for Na adsorption is −1.16 eV, whereas for CO_2 adsorption, the value is −0.08 eV. Finally, our findings reveal that Gibbs free

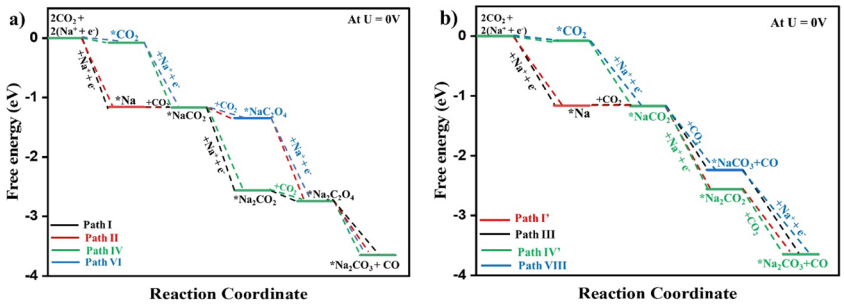

Fig. 2 Calculated energetic profiles of (a) Na_2CO_3 + CO formation *via* $Na_2C_2O_4$ intermediate and (b) direct Na_2CO_3 + CO nucleation on RuO_2 at $U = 0$ V.

energy changes for $Na_2C_2O_4$ and Na_2CO_3 + CO are −2.74 and −3.65 eV, respectively.

At the equilibrium potentials of $Na_2C_2O_4$ (U_0 ($Na_2C_2O_4$) = 2.12 V) and Na_2CO_3 + CO (U_0 (Na_2CO_3 + CO) = 2.37 V), the exothermic nature of intermediate steps involving Na adsorption and electron transfer at $U = 0$ V transitions to endothermic behavior, as illustrated by the Gibbs free energy profiles in Fig. 3a and b. This transition indicates that, at equilibrium potentials, the adsorption of Na and the associated electron transfer processes become energetically unfavorable, shifting toward endothermic behavior. Overall, the Gibbs free energy changes for final $Na_2C_2O_4$ and Na_2CO_3 + CO are 1.50 eV and 1.10 eV, respectively. The nucleation mechanisms of $Na_2C_2O_4$ and Na_2CO_3 + CO in Na–CO_2 batteries both involve critical initial and subsequent CO_2 adsorption steps on the RuO_2 substrate. In the case of $Na_2C_2O_4$ formation, the first CO_2 adsorption is slightly exothermic ($\Delta G = -0.08$ eV), yet the CO_2 molecule remains linear with negligible bond elongation, indicating that it is not activated. The second CO_2 adsorption, required for oxalate ($C_2O_4^{2-}$) formation corresponding to Path V, is thermodynamically unfavorable, with a positive free energy of +0.79 eV (as shown in Fig. S3). Furthermore, the Gibbs free energy to produce CO_3 + CO *via* Path VII is near thermoneutral ($\Delta G = -0.06$ eV)[32] when compared to the free energies of Na adsorption intermediates, as evidenced by the free energy profile in Fig. S4. Following the formation of $C_2O_4^{2-}$ and CO_3^{2-} species, subsequent Na^+ adsorption leads to the formation of NaC_2O_4 and $Na_2C_2O_4$, and $NaCO_3$ + CO and Na_2CO_3 + CO, respectively. These sodiation steps are thermodynamically favorable under standard conditions ($U = 0$ V), exhibiting negative free energies. However, at the equilibrium potential, the electrochemical steps become endothermic, with free energies of 0.07 eV and 0.72 eV for NaC_2O_4 and $Na_2C_2O_4$, and 0.28 eV and 0.96 eV for $NaCO_3$ + CO and Na_2CO_3 + CO, respectively. $C_2O_4^{2-}$ or CO_3 + CO is formed by the chemical coupling of two CO_2 species, without the need for additional electron transfer. The catalyst must adequately absorb and activate CO_2 for the reaction to be successful. In our cases, the unfavorable nature of CO_2 adsorption indicates the limitation of CO_2 activation on RuO_2. Hence, Pathways V and VII are not thermodynamically preferred, and we didn't consider them further. Based on the overall free energy pathway analysis by considering both direct and indirect (*via* oxalate path formation) carbonate formation at equilibrium potential, Paths I, I′ and II are initially competing with Path III. However, in Paths I and I′ the third step involving the electrochemical formation of Na_2CO_2 becomes uphill. In contrast, for Paths II and III, the third step is a chemical step involving the formation of NaC_2O_4 and $NaCO_3$ + CO, respectively, which are downhill in nature. Among these two pathways, Path III is more energetically favoured. The remaining pathways (IV, IV′, V, VI, VII, and VIII) involve initial and subsequent CO_2 adsorption, which is not favored. Although the initial CO_2 adsorption is marginally exothermic, the CO_2 molecule is not activated, rendering these routes non-competitive. Consequently, Path III is identified as

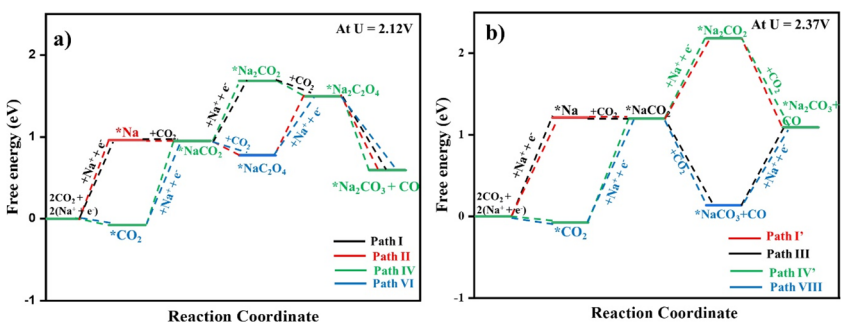

Fig. 3 Calculated energetic profiles of (a) Na_2CO_3 + CO formation *via* $Na_2C_2O_4$ intermediate and (b) direct Na_2CO_3 + CO nucleation on the RuO_2 surface at U_0 ($Na_2C_2O_4$) = 2.12 V and U_0 (Na_2CO_3 + CO) = 2.37 V.

an overall energetically preferred and therefore exclusively considered for electrochemical free energy calculations.

Wang *et al.* conducted a modeling study on Li–CO_2 batteries and found Li_2CO_3 as the final discharge product after analyzing the formation and decomposition paths.[43] Besides, the experimental work performed by Hu *et al.* found that Na_2CO_3 is the primary discharge product in Na–CO_2 batteries by employing *in situ* Raman and CO_2 evolution studies by using a Ru–CNT (ruthenium on carbon nanotube) composite cathode, validating the reversible reaction of $3CO_2 + 4Na \leftrightarrow 2Na_2CO_3 + C$.[44] Overall in our work, we found that Na_2CO_3 + CO further react with CO on the RuO_2 substrate leading to $Na_2CO_3 + C + CO_2$ with a free energy change of −2.32 eV. Hence, Na_2CO_3 + C is identified as the final discharge product in our work when using RuO_2 (211) as a catalyst. Detailed calculations of the equilibrium potentials for $Na_2C_2O_4$ and Na_2CO_3 + CO are provided in the (SI).

3.1.1 Charge transfer analysis. To gain a deeper understanding of the chemical interactions and binding mechanisms between the reaction intermediate species and the RuO_2 (211) substrate, we conducted charge transfer analysis using the Bader charge method, as illustrated in Fig. 4. A positive charge transfer value indicates electron donation from the intermediate species (Na, CO_2, $Na_2C_2O_4$ and Na_2CO_3 + CO) to the RuO_2 catalyst, while a negative value signifies electron flow from the RuO_2 substrate to the intermediate species. For the adsorption of a Na atom on RuO_2 (211), a significant positive charge transfer of 0.891 |e| was observed from Na to the catalytic surface. This substantial charge transfer indicates strong electrostatic and favorable electronic interactions between Na and RuO_2. In contrast, adsorption of a CO_2 molecule resulted in a minimal charge transfer of −0.05 |e|, indicating weak physisorption, where electrons are transferred from the RuO_2 surface to an inert CO_2 molecule. For the intermediate species such as $Na_2C_2O_4$ and Na_2CO_3 + CO a positive charge transfer of 0.362|e| and 0.154 |e|, respectively, was noted. Besides, the charge density difference (DCD) analysis was performed for Na and CO_2 on RuO_2, with the results shown in Fig. S6. The DCD analysis further supports our Bader charge transfer analysis, providing additional evidence for the significant charge transfer observed in our RuO_2 system. The PDOS analysis (Fig. S7) for adsorbed Na, $Na_2C_2O_4$, and Na_2CO_3 + CO on the RuO_2 substrate revealed that the substrate retains its intrinsic electronic conductivity upon adsorption, indicating its suitability for electrochemical applications. The minimal charge transfer for CO_2 on the RuO_2 catalyst is primarily due to the inert nature of the CO_2 molecule. CO_2 has a linear geometry and strong covalent bonds, making it chemically stable and resistant to interaction with a catalytic surface. The negligible charge transfer correlates with the inactivation of the adsorbed CO_2 molecule, contributing to a higher energy barrier for the formation of $Na_2C_2O_4$, and Na_2CO_3 + CO intermediate species.

3.2 Electrochemical free energy profile for CO_2 reduction

To comprehensively assess the electrochemical performance, we probed the cathode reactions employing the two-electron reaction mechanisms throughout the discharging (CO_2RR)/charging (CO_2ER) processes in Na–CO_2 batteries. Based on the thermodynamic screening outlined in Section 3.1, we focus only on Path III for the electrochemical free energy analysis, as it represents the most energetically favorable CO_2 reduction pathway at equilibrium potential. The electrochemical free energy plot, as depicted in Fig. 5, intricately illustrates the spontaneous and downhill nature of the electrochemical free energies at $U = 0$ V, showcasing that all reaction steps exhibit $\Delta G < 0$ V. During the discharge process, the electrochemical free energy profile remains downhill until the electrode potential reaches 1.43 V. As a result, the RuO_2 substrate exhibits a discharge overpotential of 1.56 V. Furthermore, it was found that the potential determining step in the overall discharge process is the third step, where the electrochemical electron transfer for the conversion of $NaCO_3$ to Na_2CO_3 becomes energetically uphill.

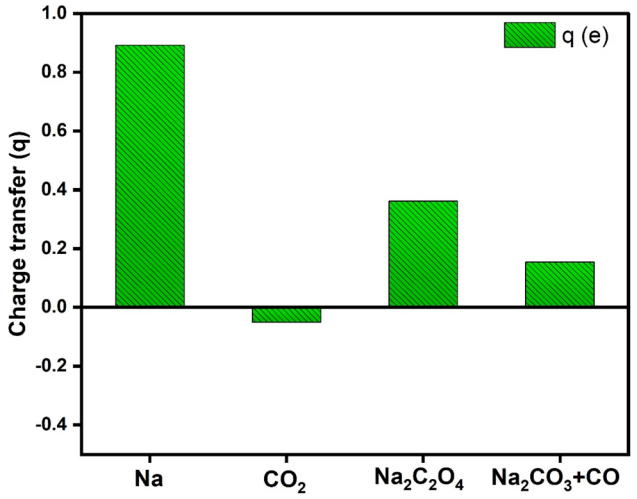

Fig. 4 Computed charge transfer q(e) for various reactants adsorbed on the RuO_2 surface.

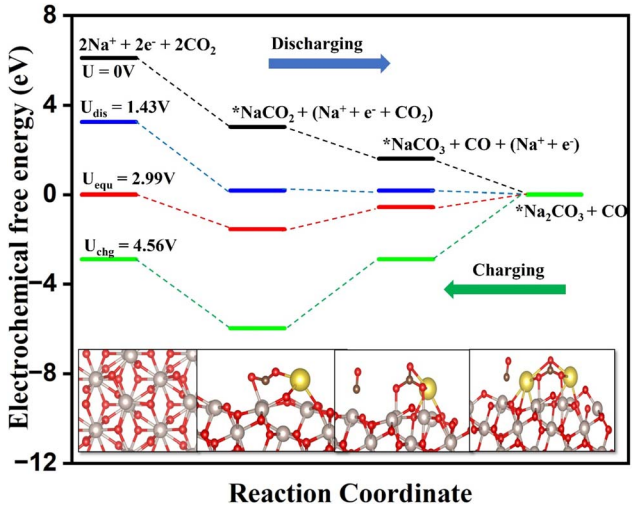

Fig. 5 Electrochemical free energy change during discharging/charging for the most favorable pathway using the RuO_2 (211) catalyst.

The RuO_2 substrate's electrochemical free energy profile remains downward during the charging process until the charging potential decreases to 4.56 V. Thus, 1.57 V is found to be the charging overpotential. The potential-controlling step during charging corresponds to the decomposition of Na_2CO_3 + CO, accompanied by electron transfer. The catalytic activity of the bifunctional catalyst for the CO_2RR/CO_2ER is evaluated using the total overpotential, with smaller values indicating superior activity. The total overpotential for the electrochemical reaction in Na–CO_2 batteries with the RuO_2 substrate is calculated to be 3.13 V.

3.3 CO_2 capture and regeneration using PDA

The high charge and discharge overpotentials calculated for the RuO_2 catalyst primarily stem from the limited activation of CO_2, which motivates us to further investigate potential mechanisms for its pre-activation prior to electrocatalytic reduction on the electrode surface. To address this issue, PDA was introduced into the electrolyte as a molecular co-adsorbent. The primary role of PDA in the electrolyte is to capture and activate CO_2 molecules by donating electrons. This interaction involves the donation of electrons from the nitrogen's (N) lone pairs to the CO_2 molecule, resulting in a significant change in the CO_2 bond angles and bond lengths, indicative of a more reactive configuration. In this study, we focus on the impact of PDA amine on CO_2 reaction kinetics, particularly in the context of Na–CO_2 batteries. To the best of our knowledge, this work represents the first systematic investigation of PDA's role in Na–CO_2 batteries. Analysis of the binding energy of CO_2 on PDA amine reveals the spontaneous binding of CO_2 (−0.35 eV), facilitated by the lone pair donation from the nitrogen atom of the amino group to the electrophilic carbon (C_4^+) of CO_2. This binding results in the activation of CO_2 molecule, evidenced by the elongation of the C═O bond from 1.16 Å to 1.26 Å and a bending of the O–C–O bond angle to 124°. The configurations are shown in Fig. 6. The activation of CO_2 by PDA ($C_3H_{10}N_2$), represented by its reactive primary amine site (denoted as RNH_2), facilitates the formation of neutral carbamic acid (RNHCOOH) with an exothermic Gibbs free energy change of −0.43 eV, demonstrating the effectiveness of PDA in CO_2 capture.

To further elucidate how PDA interacts with CO_2, we carried out Natural Bond Orbital (NBO) analysis using Gaussian 16 (G-16) to evaluate the charge distribution in CO_2 before and after its binding with PDA. In the gas phase, the carbon atom in CO_2 exhibited a partial positive charge of +1.02|e|, indicating its electrophilic nature. Upon interaction with PDA, the charge on the carbon center decreased to +0.886|e|, suggesting electron donation from PDA to CO_2. Similarly, the N atom in pristine PDA showed a partial negative charge of −0.90|e|. After complexation with CO_2, this value shifted to −0.67|e|, indicating a loss of electron density due to charge transfer from N to the CO_2 molecule. Corresponding results are presented in Fig. S5. In addition to NBO analysis, the electronic structure of gaseous CO_2 and the CO_2–PDA complex was investigated. The energy band gap, defined as the difference between the LUMO and HOMO energies, was calculated to be 9.89 eV for isolated CO_2 and 6.26 eV for the CO_2–PDA complex. This significant reduction in the band gap upon complex formation indicates strong electronic interaction and orbital hybridization between CO_2 and PDA.

In the context of amine-based CO_2 capture and conversion, our findings build upon previous work in dimethyl sulfoxide (DMSO), where CO_2 absorption by 2-ethyoxyethylamine (EEA) led to the stabilization of carbamic acid.[5] The introduction of $LiClO_4$ salt then facilitated the conversion of carbamic acid to lithium carbamate. Our study expands this understanding by predicting the Gibbs free energy for the formation of carbamate ($RNHCOO^-$) in the presence and absence of Na^+ cations. We found that the deprotonation of carbamic acid to form ammonium carbamate ($RNHCOO^-$ and RNH_3^+) results in a substantial endothermic free energy change of 1.15 eV. However, the introduction of Na^+ cations markedly alters the thermodynamics, lowering the free energy for sodium carbamate (RNHCOONa) formation to 0.12 eV. This underscores the importance of ion association in facilitating the carbamic acid-to-carbamate conversion process. Notably, experimental results showed that the alkali-metal cations have a significant impact on amine–CO_2 adduct speciation, stabilizing carbamate species more effectively due to stronger cation–carbamate interactions.[24] Moreover, our study delves into the N–C bond cleavage energy in amine-based CO_2 capture, a critical step for the regeneration of amines and overcoming the energy-intensive challenges of thermal cleavage. The N–C bond cleavage, which produces RNH_2 and $NaCO_2$, is slightly exothermic in the electrolyte bulk (−0.6 eV); however, at the RuO_2 catalytic cathode interface, the reaction becomes significantly more exothermic (−6.38 eV). This high exothermicity is attributed to the altered electronic environment, enhanced local coordination effects, and catalytic sites on the electrode surface, all of which contribute to the cleavage of the N–C bond and the subsequent regeneration of amines near the electrode surface (Fig. 7).

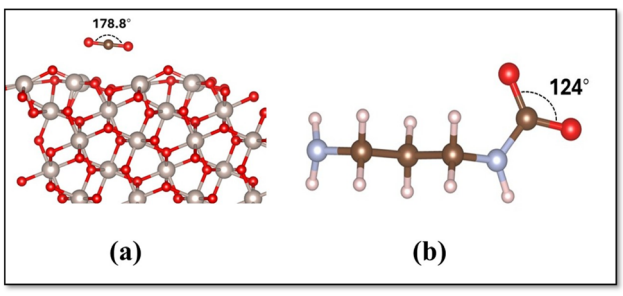

Fig. 6 Comparison of CO_2 molecular geometry in two environments: (a) linear geometry of a gaseous CO_2 molecule adsorbed on the RuO_2 substrate; (b) bent geometry of CO_2 in the presence of PDA.

3.4 Electrochemical free energy profile with PDA

To evaluate the electrochemical performance, we examined the two-electron reaction mechanisms at the cathode interface during the discharging (CO_2RR) and charging (CO_2ER) processes in Na–CO_2 batteries using RuO_2 as the cathode catalyst and PDA-based electrolyte as a reaction medium. At U =

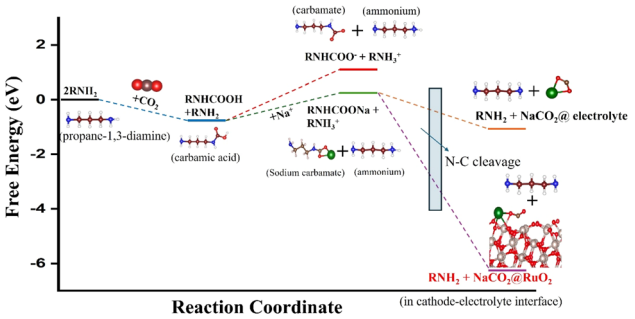

Fig. 7 Free energy profile illustrating CO_2 capture by PDA and subsequent regeneration of RNH_2.

0 V, where all reaction steps exhibit ΔG <0 V, the electrochemical free energy profile (Fig. 8) shows exothermic reaction steps. Throughout the discharge process, the free energy profile remains downhill until the electrode potential attains 1.64 V, resulting in a calculated discharge overpotential of 1.21 V. Importantly, the third step, which entails the electrochemical electron transfer for transitioning $NaCO_3$ to Na_2CO_3 + CO, turns energetically uphill as the electrode potential rises, suggesting that this step controls the discharge process.

During the charging process, the electrochemical free energy profile continues to decline until the charging potential drops to 4.08 V, which relates to a charge overpotential of 1.23 V. The decomposition of Na_2CO_3 + CO is determined to be a potential determining step in the entire charging process. Overall, the inclusion of PDA greatly reduced both discharge and charge overpotentials in comparison to pristine RuO_2, thereby improving bifunctional catalytic performance (Table 1). The PDA-assisted system lowers the total overpotential to 2.44 V compared to 3.13 V for the pristine RuO_2 value. This demonstrates that PDA improves the electrochemical conversion of CO_2 in Na–CO_2 batteries. Consistent with our findings, previous

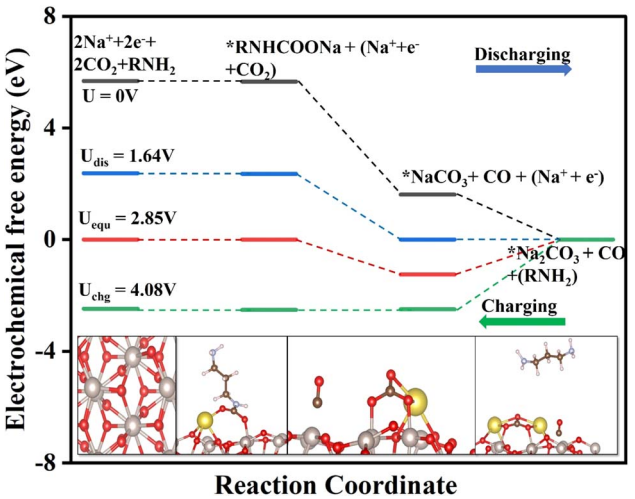

Fig. 8 Electrochemical free energy changes associated with the most favorable discharge and charge pathway on the RuO_2 (211) catalyst in the presence of PDA.

Table 1 Calculated overpotential for the most favorable electrochemical free energy pathway for Na_2CO_3 nucleation with and without PDA

	Without PDA	With PDA
Equilibrium potential (V)	2.99	2.85
Charge overpotential (V)	1.57	1.23
Discharge overpotential (V)	1.56	1.21
Total overpotential (V)	3.13	2.44

experimental studies have demonstrated that amine-mediated CO_2 chemistry efficiently reduces overpotential and enhances reversibility in M–CO_2 batteries. For example, research by Wang *et al.* showed that the introduction of tetraethylenepentamine (TEPA) significantly reduced the charge overpotential with improved electrochemical reversibility in the Li–CO_2 system.[45] The TEPA-containing Li–CO_2 battery had a lower overpotential (4.50 V) compared to a battery without TEPA (4.91 V). Besides, the introduction of PDA as an electrolyte additive in the Mg–CO_2 system showed high-rate performance and better cycling stability with an observed overpotential of 1.50 V.[46] The schematic illustration of the most favorable reaction pathway involving amine adducts that leads to the formation of Na_2CO_3 + CO is presented in Fig. S8, and the detailed methodology for calculating the electrochemical free energy change is also provided in the SI.

4. Conclusions

In summary, we used DFT calculations to systematically investigate the mechanisms of CO_2 reduction in the Na–CO_2 system. The computed free energy profiles confirm that Na_2CO_3 is the final discharge product on the RuO_2 substrate. CO_2 was found not to be activated on the RuO_2 catalyst, as evidenced by the negligible charge transfer RuO_2 to CO_2, revealed through Bader charge analysis. To address this limitation, we introduced PDA as an electrolyte additive, which significantly enhanced CO_2 activation. This was evidenced by a reduction in the CO_2 bond angle from 180° to 124°, an elongation of the C=O bond length from 1.16 to 1.26 Å, and substantial charge transfer from the nitrogen atoms in PDA to the carbon atom of CO_2. Gibbs free energy calculations using an implicit solvation model showed that amine regeneration *via* N–C cleavage is more favored at the RuO_2 substrate than in the bulk electrolyte, which illustrates accelerated CO_2 conversion kinetics at the electrode–electrolyte interface. Additionally, PDA exhibited spontaneous binding with CO_2 (−0.35 eV), which further facilitates its adsorption and activation at the electrode surface. The PDA-assisted systems also achieved a significant reduction in both charge and discharge overpotentials, from 1.57 to 1.23 V and from 1.56 to 1.21 V, respectively. Overall, our findings establish PDA-assisted RuO_2 as an effective substrate–additive combination that enhances CO_2 activation, promotes amine regeneration, and improves electrochemical performance in Na–CO_2 batteries. This work provides a fundamental understanding of CO_2 capture and conversion mechanisms and demonstrates the

promise of molecularly engineered additives for next-generation energy storage systems.

Conflicts of interest

There are no conflicts of interest to declare.

Data availability

The authors confirm that the data required to reproduce the findings of this study are available within the article and can be reproduced by density functional theory calculations.

Supplementary information (SI): optimized geometric configurations for favourable nucleation pathways, free-energy profiles, NBO analysis, DCD, PDOS plots, equilibrium voltage calculations, and detailed procedures for electrochemical free-energy calculations. See DOI: https://doi.org/10.1039/d5ta09674j.

Acknowledgements

This work was supported by the National Science Foundation (NSF) CAREER Award (CBET-2441420).

References

1 X. Mu, P. He and H. Zhou, *Acc. Mater. Res.*, 2024, **5**, 467–478.
2 G. T. Rochelle, *Science*, 2009, **325**, 1652–1654.
3 D. J. Heldebrant, P. K. Koech, V.-A. Glezakou, R. Rousseau, D. Malhotra and D. C. Cantu, *Chem. Rev.*, 2017, **117**, 9594–9624.
4 M. E. Boot-Handford, J. C. Abanades, E. J. Anthony, M. J. Blunt, S. Brandani, N. M. Dowell, J. R. Fernández, M.-C. Ferrari, R. Gross, J. P. Hallett, R. Stuart Haszeldine, P. Heptonstall, A. Lyngfelt, Z. Makuch, E. Mangano, R. T. J. Porter, M. Pourkashanian, G. T. Rochelle, N. Shah, J. G. Yao and P. S. Fennell, *Energy Environ. Sci.*, 2014, **7**, 130–189.
5 A. Khurram, M. He and B. M. Gallant, *Joule*, 2018, **2**, 2649–2666.
6 O. S. Bushuyev, P. D. Luna, C. T. Dinh, L. Tao, G. Saur, J. van de Lagemaat, S. O. Kelley and E. H. Sargent, *Joule*, 2018, **2**, 825–832.
7 R. J. Lim, M. Xie, M. A. Sk, J.-M. Lee, A. Fisher, X. Wang and K. H. Lim, *Catal. Today*, 2014, **233**, 169–180.
8 S. Garg, M. Li, A. Z. Weber, L. Ge, L. Li, V. Rudolph, G. Wang and T. E. Rufford, *J. Mater. Chem. A*, 2020, **8**, 1511–1544.
9 C. Costentin, M. Robert and J.-M. Savéant, *Chem. Soc. Rev.*, 2013, **42**, 2423–2436.
10 F. Wang, Y. Li, X. Xia, W. Cai, Q. Chen and M. Chen, *Adv. Energy Mater.*, 2021, **11**, 2100667.
11 J. Xie, Z. Zhou and Y. Wang, *Adv. Funct. Mater.*, 2020, **30**, 1908285.
12 A. Khurram, PhD Thesis, Massachusetts Institute of Technology, Department of Mechanical Engineering, 2020.
13 Z. Wang, C. Sun, L. Lu and L. Jiao, *Batteries*, 2023, **9**, 36.
14 W.-J. Li, C. Han, W. Wang, F. Gebert, S.-L. Chou, H.-K. Liu, X. Zhang and S.-X. Dou, *Adv. Energy Mater.*, 2017, **7**, 1700274.
15 V. Palomares, P. Serras, I. Villaluenga, K. B. Hueso, J. C. González and T. Rojo, *Energy Environ. Sci.*, 2012, **5**, 5884–5901.
16 C. Xia, R. Black, R. Fernandes, B. Adams and L. F. Nazar, *Nat. Chem.*, 2015, **7**, 496–501.
17 X. Hu, J. Sun, Z. Li, Q. Zhao, C. Chen and J. Chen, *Angew. Chem., Int. Ed.*, 2016, **55**, 6482–6486.
18 M. Okoshi, Y. Yamada, A. Yamada and H. Nakai, *J. Electrochem. Soc.*, 2013, **160**, A2160.
19 D. Sui, M. Chang, H. Wang, H. Qian, Y. Yang, S. Li, Y. Zhang and Y. Song, *Catalysts*, 2021, **11**, 603.
20 S. Thoka, Z. Tong, A. Jena, T.-F. Hung, C.-C. Wu, W.-S. Chang, F.-M. Wang, X.-C. Wang, L.-C. Yin, H. Chang, S.-F. Hu and R.-S. Liu, *J. Mater. Chem. A*, 2020, **8**, 23974–23982.
21 E. Lamy, L. Nadjo and J. M. Saveant, *J. Electroanal. Chem. Interfacial Electrochem.*, 1977, **78**, 403–407.
22 Z. Zhang, X.-G. Wang, X. Zhang, Z. Xie, Y.-N. Chen, L. Ma, Z. Peng and Z. Zhou, *Advanced Science*, 2018, **5**, 1700567.
23 S. R. Gowda, A. Brunet, G. M. Wallraff and B. D. McCloskey, *J. Phys. Chem. Lett.*, 2013, **4**, 276–279.
24 A. Khurram, L. Yan, Y. Yin, L. Zhao and B. M. Gallant, *J. Phys. Chem. C*, 2019, **123**, 18222–18231.
25 B. Gallant, *Removing CO_2 from power plant exhaust*, MIT News, 2019, https://news.mit.edu/2019/removing-co2-from-power-plant-exhaust-0729.
26 C.-C. Wang, *J. Phys. Chem. C*, 2009, **113**, 2816–2821.
27 C.-C. Wang, Y.-J. Yang, J.-C. Jiang, D.-S. Tsai and H.-M. Hsieh, *J. Phys. Chem. C*, 2009, **113**, 17411–17417.
28 M. Karamad, H. A. Hansen, J. Rossmeisl and J. K. Nørskov, *ACS Catal.*, 2015, **5**, 4075–4081.
29 L. Zhang, H. Jang, H. Liu, M. G. Kim, D. Yang, S. Liu, X. Liu and J. Cho, *Angew. Chem.*, 2021, **133**, 18969–18977.
30 Q. Liang, A. Bieberle-Hütter and G. Brocks, *J. Phys. Chem. C*, 2022, **126**, 1337–1345.
31 Y. Wang, R. Yang, Y. Ding, B. Zhang, H. Li, B. Bai, M. Li, Y. Cui, J. Xiao and Z.-S. Wu, *Nat. Commun.*, 2023, **14**, 1412.
32 R. Jayan and M. M. Islam, *ACS Appl. Mater. Interfaces*, 2023, **15**, 45895–45904.
33 G. Kresse and J. Furthmüller, *Phys. Rev. B:Condens. Matter Mater. Phys.*, 1996, **54**, 11169–11186.
34 J. P. Perdew, K. Burke and M. Ernzerhof, *Phys. Rev. Lett.*, 1996, **77**, 3865–3868.
35 S. Chen, H. Huang, P. Jiang, K. Yang, J. Diao, S. Gong, S. Liu, M. Huang, H. Wang and Q. Chen, *ACS Catal.*, 2020, **10**, 1152–1160.
36 K. Mathew, R. Sundararaman, K. Letchworth-Weaver, T. A. Arias and R. G. Hennig, *J. Chem. Phys.*, 2014, **140**, 084106.
37 A. Kopač Lautar, J. Bitenc, T. Rejec, R. Dominko, J.-S. Filhol and M.-L. Doublet, *J. Am. Chem. Soc.*, 2020, **142**, 5146–5153.
38 V. Wang, N. Xu, J.-C. Liu, G. Tang and W.-T. Geng, *Comput. Phys. Commun.*, 2021, **267**, 108033.
39 K. Momma and F. Izumi, *J. Appl. Crystallogr.*, 2011, **44**, 1272–1276.

40 M. J. Frisch, G. W. Trucks, H. B. Schlegel, G. E. Scuseria, M. A. Robb, J. R. Cheeseman, G. Scalmani, V. Barone, G. A. Petersson, H. Nakatsuji, X. Li, M. Caricato, A. V. Marenich, J. Bloino, B. G. Janesko, R. Gomperts, B. Mennucci, H. P. Hratchian, J. V. Ortiz, A. F. Izmaylov, J. L. Sonnenberg, D. Williams-Young, F. Ding, F. Lipparini, F. Egidi, J. Goings, B. Peng, A. Petrone, T. Henderson, D. Ranasinghe, V. G. Zakrzewski, J. Gao, N. Rega, G. Zheng, W. Liang, M. Hada, M. Ehara, K. Toyota, R. Fukuda, J. Hasegawa, M. Ishida, T. Nakajima, Y. Honda, O. Kitao, H. Nakai, T. Vreven, K. Throssell, J. A. Montgomery Jr, J. E. Peralta, F. Ogliaro, M. J. Bearpark, J. J. Heyd, E. N. Brothers, K. N. Kudin, V. N. Staroverov, T. A. Keith, R. Kobayashi, J. Normand, K. Raghavachari, A. P. Rendell, J. C. Burant, S. S. Iyengar, J. Tomasi, M. Cossi, J. M. Millam, M. Klene, C. Adamo, R. Cammi, J. W. Ochterski, R. L. Martin, K. Morokuma, O. Farkas, J. B. Foresman and D. J. Fox, *Gaussian 16*, Gaussian, Inc., Wallingford CT, 2016.
41 X. Hu, P. H. Joo, E. Matios, C. Wang, J. Luo, K. Yang and W. Li, *Nano Lett.*, 2020, **20**, 3620–3626.
42 B. Xu, D. Zhang, S. Chang, M. Hou, C. Peng, D. Xue, B. Yang, Y. Lei and F. Liang, *Cell Rep. Phys. Sci.*, 2022, **3**, 100973.
43 Y. Wang, L. Hao and M. Bai, *J. Solid State Electrochem.*, 2021, **25**, 2571–2585.
44 X. Hu, J. Sun, Z. Li, Q. Zhao, C. Chen and J. Chen, *Angew. Chem., Int. Ed.*, 2016, **55**, 6482–6486.
45 Y. Wang, X. Chen, Y. Mao, Y. Luo, B. Sun, Q. Zhang and J. Xie, *J. Phys. Chem. Lett.*, 2025, **16**, 6266–6272.
46 C. Peng, L. Xue, Z. Zhao, L. Guo, C. Zhang, A. Wang, J. Mao, S. Dou and Z. Guo, *Angew. Chem.*, 2024, **136**, e202313264.